GEOPHYSICS, VOL. 86, NO. 1 (JANUARY-FEBRUARY 2021); P. IM1–IM14, 15 FIGS., 2 TABLES.
10.1190/GEO2019-0832.1

DOI:10.1190/geo2019-0832.1

Improving fault surface construction with inversion-based methods

Zhengfa Bi[1] and Xinming Wu[1]

ABSTRACT

Constructing fault surfaces is a key step for seismic structural interpretation and building structural models. We automatically construct fault surfaces from oriented fault samples scanned from a 3D seismic image. The main challenges of the fault surface construction include the following: Some fault samples are locally missing, the positions and orientations of the fault samples may be noisy, and surfaces may form complicated intersections with each other. We adopt the Poisson equation surface method (PESM) and the point-set surface method (PSSM) to automatically construct complete fault surfaces from fault samples and their corresponding orientations. Our methods can robustly fit the noisy fault samples and reasonably fill holes or missing samples, thus improving fault surface construction. By formulating fault surface construction as an inverse problem, we estimate a scalar function to approximate the fault samples in the least-squares sense. In PESM, we estimate the scalar function by solving a weighted Poisson equation. In PSSM, the scalar function is derived by fitting local algebraic spheres based on moving least-squares approximations. Then, the fault surfaces can be approximated by zero isosurfaces of the resulting scalar function. To handle complicated cases of crossing faults, we first classify the fault samples according to their orientations, and we take each class of samples as input of our inversion-based approaches to independently construct the crossing faults. We determine the ability of our methods in robustly building the complete fault surface using synthetic and real seismic images complicated by noise and complexly intersecting faults.

INTRODUCTION

Faults are often considered important geologic surfaces to control the boundary of seismic horizons or to reduce risk in well placement in reservoir exploration. Constructing 3D fault surfaces from calculated fault attributes is a key step in seismic interpretation for geologic structures. Although a seismic image incorporates rich stratigraphic and structural features, most are dominated by the features of seismic reflections, whereas faults are typically displayed as reflection discontinuities. Therefore, fault interpretation requires us to compute a set of additional images in which fault features are highlighted while reflections and others are suppressed. To extract fault surfaces, we first estimate fault attributes, which allow better visualization of geologic features about fault positions and orientations (strikes and dips).

Various approaches have been proposed to calculate fault images to detect faults by measuring seismic reflection continuity or discontinuity. Several approaches are based on reflection continuities such as semblance (Marfurt et al., 1998; Lou et al., 2019a) and coherency (Marfurt et al., 1999; Li and Lu, 2014; Qi et al., 2017a) or reflection discontinuities such as variance (Van Bemmel and Pepper, 2000; Randen et al., 2001), curvature (Roberts, 2001; Al-Dossary and Marfurt, 2006; Di and Gao, 2014b, 2016), and gradient magnitude (Aqrawi and Boe, 2011). However, these attributes are also prone to the features unrelated to faults such as stratigraphic features or incoherent data noise. For this reason, a measure of continuity or discontinuity is insufficient to accurately detect faults (Hale, 2013).

Considerably more progress has been made to improve the quality of fault attributes estimated from a seismic image. Qi and Castagna (2013) detect faults in the Barnett Shale by using principal component analysis in the seismic attribute images. Zhang et al. (2014) use a vein pattern recognition algorithm to improve coherence attributes. Di and Gao (2014a) suggest implementing a gray-level transformation and the Canny edge detector for improved imaging of discontinuities to enhance visualization for structural and stratigraphic details. Qi et al. (2017b, 2018) build a workflow to

Manuscript received by the Editor 24 December 2019; revised manuscript received 5 September 2020; published ahead of production 1 October 2020; published online 30 December 2021.
[1]University of Science and Technology of China, School of Earth and Space Sciences, Hefei 230026, China. E-mail: zfbi@mail.ustc.edu.cn; xinmwu@ustc.edu.cn (corresponding author).

DOI:10.1190/geo2019-0832.1

enhance coherence images along with fault extensions and improve the accuracy and completeness of subtle discontinuities in a noisy seismic image. Lou et al. (2019b) eliminate the staircase artifacts and undesired stratigraphic anomalies by using a local fault model. In addition, recently proposed machine learning methods can estimate fault attributes from seismic data (Huang et al., 2017; Di et al., 2018; Guitton, 2018; Xiong et al., 2018; Zhao and Mukhopadhyay, 2018; Wu et al., 2019a).

For accurately distinguishing faults from other noisy features, we follow the approach developed in Hale (2013) and Wu and Hale (2016), in which the fault likelihood is computed by smoothing the numerator and denominator of the semblance over all possible combinations of fault strikes and dips. Fault-oriented smoothing is useful to enhance fault features and suppress noisy features (unrelated to faults) in the calculated fault likelihood image. When computing the fault likelihood, we can simultaneously estimate the strike and dip attributes that provide the local fault strike and dip even at a sample location without faults. For a 3D seismic image, we only estimate one fault likelihood image as well as two fault orientation images of the strike and dip.

With the fault attributes of likelihood, strike, and dip, we can further construct fault surfaces. Pedersen et al. (2002) and Pedersen et al. (2003) propose an ant-tracking approach to recover fault segments and then merge into a set of larger fault surfaces. Similarly, some other authors (Gibson et al., 2005; Admasu et al., 2006; Kadlec et al., 2008) suggest building a major fault surface from smaller patches. Hale (2013) considers the fault surface as a quadrilateral mesh that coincides with the ridges of the fault likelihood. Wu and Hale (2016) introduce a link-data structure to construct fault surfaces by connecting each fault sample with immediately adjoining neighbors if they have similar attributes. Thus, fault surfaces reconstructed in this way are linked sets of fault samples. A single fault sample can be displayed as a square oriented by strike and dip angles and colored by fault likelihood such that the linked fault sample sets appear to be continuous surface by enlarging the size of each sample. Wu and Fomel (2018) point out that fault surfaces can be constructed from a fault probability image by extracting the maximum surface with a dynamic programming algorithm. Although numerous automatic methods have been proposed for constructing fault surfaces, significant human interaction is still essential in constructing complete fault surfaces without holes when building complex crossing fault systems.

In this study, we propose two inversion-based methods to automatically construct a triangulated approximation of complete fault surfaces from fault samples and their corresponding orientations. Our methods can robustly fit the noisy fault samples while reasonably filling holes or missing samples, and they can thus improve fault surface construction. In our methods, we first use the fault-scanning method (Hale, 2013; Wu and Hale, 2016) to simultaneously compute three attribute images of the fault likelihood, strike, and dip from a seismic image. With the three computed fault attributes, we define oriented fault samples at the ridges of the fault likelihood image. We subsequently construct fault surfaces from the oriented fault samples by two inversion-based surface construction methods. Instead of directly linking the fault samples to construct fault surfaces as discussed by Wu and Hale (2016), we first compute a spatially continuous scalar function by solving a simple linear equation that is constructed with the positions and orientations of all of the input fault samples. Then, we extract the fault surfaces from the zero isosurfaces of the scalar function by using the marching cubes method (Lorensen and Cline, 1987). We find that the proposed methods are capable of constructing complete fault surfaces by reliably fitting noisy fault samples and reasonably filling holes or missing samples. In addition, the calculated scalar function can be transformed into any format of the data structure to flexibly display fault surfaces.

To further handle the complicated cases of building crossing faults, we exploit a clustering method to automatically classify the fault samples according to their orientations. Then, we take each class of fault samples as the input of our inversion-based methods to independently compute the scalar function and extract the fault surfaces. We verify the effectiveness of our inversion-based fault surface construction methods with synthetic examples complicated by noise, crossing faults, and highly curved conical faults. We further apply our methods to the field data applications, and we find that they can automatically construct complete fault surfaces without any holes even near fault intersections. Before demonstrating the methods, we first list all of the terminologies mentioned in this study and their corresponding explanations in Table 1.

Table 1. The terminologies used in this study and the corresponding explanations.

Terminology	Explanation
Fault skin	A set of linked fault samples
Fault sample	An objective with location, orientation, and fault likelihood
Fault surface	A triangulated approximation of the fault surface
Fault attribute	Fault orientation and fault likelihood
Fault likelihood	The probability that a fault exists
Fault orientation	The normal direction of a fault (determined by the strike and dip)

ORIENTED FAULT SAMPLES

Computing fault samples and their orientation, referred to as oriented fault samples in this paper, consists of two main steps, scanning and thinning. In what follows, we describe these two steps in more detail.

Scanning for fault attributes

To highlight faults in a seismic image (such as Figure 1a), we use a fault scanning method (Hale, 2013; Wu and Hale, 2016) to look for faults in which they are typically computed as the reflection or the locally planar discontinuities. The fault scanning method detects the faults by measuring locally planar discontinuity over a given range of orientations everywhere until seeking one that can maximize the fault likelihood. In general, a smoothing filter along an actual direction of fault extension can produce the maximum smoothing response. The maximum fault likelihood and the corresponding orientation (strike and dip) are recorded at every seismic point, such that we obtain three fault attributes of the fault likelihood (Figure 1b), strike (Figure 1c), and dip (Figure 1d) simultaneously.

We find that the fault likelihood image highlights most of the fault features in a seismic

image. However, it is still challenging to construct fault surfaces because attribute estimation is often sensitive to noise or stratigraphic features. Many spurious fault features (indicated by the arrows in Figure 1b) are enhanced with high likelihoods, which significantly blurs the next surface construction. In addition, a basic assumption of the scanning method is that one seismic image point exactly corresponds to one fault sample. However, that is no longer valid for a complicated intersected fault system. For example, except for a major fault, the likelihood values in other crossed directions can also be high enough to be interpreted as faults, but they are not incorporated in the computed attribute images. Because one cannot completely obtain the fault samples near the fault intersections, the constructed fault surfaces thus suffer from holes or missing samples.

Thinning for fault samples

In the fault likelihood image, the attribute features with relatively high values can indicate locations where faults exist. However, we may not expect faults to be depicted as thick as the attribute features shown in the fault likelihood image (Figure 1b). To enhance the visibility of faults, we further apply a nonmaximum suppression to thin the fault attributes so that they are more easily interpreted. As displayed in Figure 2a, we preserve the values on the ridges of the fault likelihood attribute and set elsewhere to be zero to obtain a thinned image. In the meantime, we preserve the strikes and dips at the nonzero samples of fault likelihood to obtain the corresponding thinned strike and dip attributes (Figure 2b and 2c). We construct the oriented fault samples (Figure 2d) from those thinned images, which have nonzero values only for the samples that might be on faults, although they also can be obtained from a seismic image by using machine learning (Wu et al., 2019a, 2019b).

In this way, a fault sample incorporates three attributes of strike, dip, and likelihood all at once. We display each fault sample as a spatially oriented and colored square in Figure 2d and 2e. Its orientation is determined by the strike and dip angles, and its color represents the fault likelihood value. The right column of Figure 2e shows a close-up view of the fault samples (displayed as the oriented and colored squares) within the rectangular box in the left column of Figure 2e. We observe that some fault samples are locally missing (highlighted by the arrows in Figure 1e). In this study, our fault surface construction approaches are proposed to recover the fine geometric details of the fault surfaces guided by those fault samples and their corresponding orientations.

However, the fault scanning method might produce false fault orientations so that some nonzero samples might be unrelated to faults. Usually, the spurious fault samples have relatively low fault likelihood and cannot be connected to form a locally planar surface with significant size. As shown in Figure 2d, it is still hard to construct fault surfaces directly from such noisy fault sample sets because some misaligned samples with low fault likelihoods might be more associated with data-incoherent noise or stratigraphic features. To not only derive an improved detection of faults but to also im-

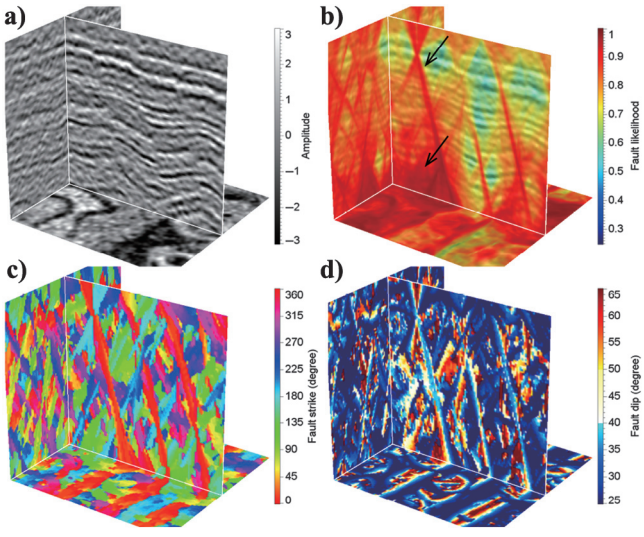

Figure 1. (a) A synthetic seismic image displayed with the fault attributes of (b) likelihood, (c) strike, and (d) dip computed using the fault scanning method. This method, like many other fault detection methods, can detect most faults but also yields many noisy features (unrelated to faults and highlighted by the arrows) in the fault attributes from which fault surface extraction remains a highly challenging task.

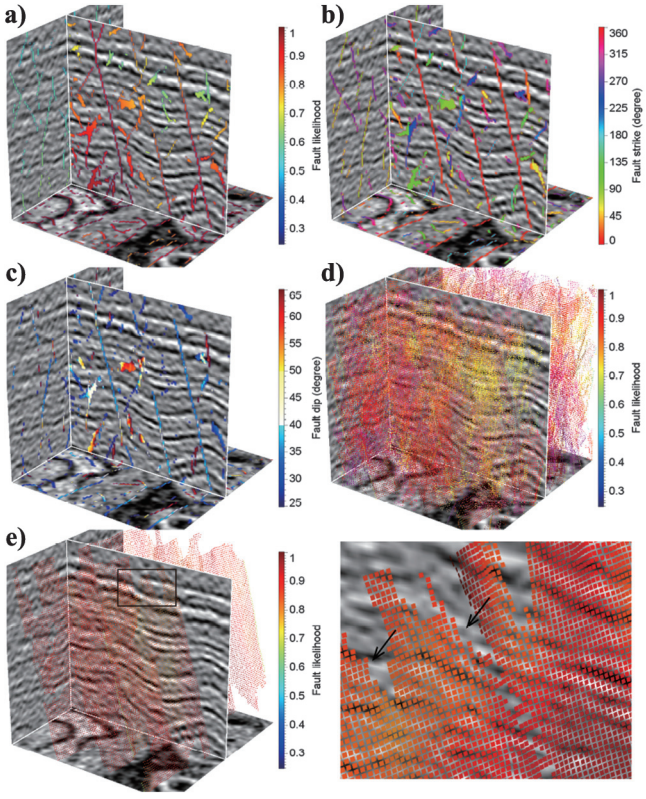

Figure 2. The thinned fault attribute image and the extracted fault samples. To enhance the seismic features of faults, we apply a structure-oriented filter to thin the three fault attributes (Figure 1b–1d) so that the faults are easier to recognize. Thus, we obtain the corresponding thinned fault attributes in (a-c), respectively. The fault samples (d) can be constructed from the thinned fault attributes, but challenges still exist because the positions and orientations of the fault samples are noisy. To filter spurious samples, we preserve the fault samples that are locally aligned to planar surfaces shown in (e). The fault samples can be visualized as oriented squares colored by fault likelihoods and oriented by strike and dip angles. The close-up view in the rectangle box in (e) displays fault samples as the set of tiny oriented squares.

DOI:10.1190/geo2019-0832.1

prove the surface construction, an extra step is required to eliminate these spurious fault samples.

FAULT SURFACE CONSTRUCTION

Highlighting fault positions or computing fault samples from attribute images is only the basic step in fault interpretation. The further step of fault surface construction is still not trivial because fault samples are often noisy and fault geometry can be highly complicated in spatial dimensions. It takes extra effort to look for structural relations among those fault samples for the next surface construction. In this study, we focus on solving the optimization problem of fault surface construction by fitting the oriented fault samples. These fault samples can be calculated from fault attributes such as the fault likelihood, or even directly from a seismic image using machine learning. For the purpose of demonstration, we exploit a classic scanning method to compute the fault samples, which are then provided to construct fault surfaces.

A key ingredient of this study is to exploit an implicit surface representation and solve for a continuous approximation to the oriented fault samples. For this reason, we formulate the fault surface construction into an optimization problem, in which fault surfaces are robustly constructed by estimating a spatially continuous scalar function. Instead of linking fault samples within a local field to form surfaces (Wu and Hale, 2016), our methods are proposed to find a globally optimum solution capable of best fitting all of the fault samples and robustly agreeing with the noisy data. We find that they offer a more accurate approximation quality to the input fault samples, and they construct faults without any holes apparent on surfaces even with noisy or locally missing fault samples.

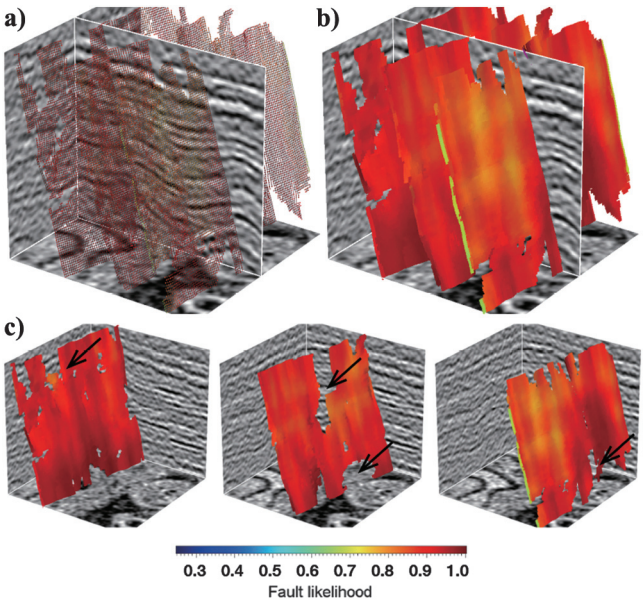

Figure 3. Fault surface construction using SGM. Linking the nearby fault samples in Figure 2e forms three fault skins (a) that consist of the linked fault samples. The fault skins can be displayed as continuous fault surfaces in (b and c) by enlarging the size of each fault sample so that they are overlapped with each other. However, each single constructed surface in (c) contains holes (highlighted by the arrows) due to locally missing samples.

In this section, we begin with a brief introduction of the link-data structure used in the surface growing approach. By creating the link-data structure, spurious fault samples can be excluded from the next fault surface construction. Then, we use the two proposed approaches to robustly construct more complete fault surfaces by estimating an implicit scalar function from the input fault samples and their corresponding orientations.

Surface growing method

With the three attribute images of fault likelihood, strike, and dip, fault surfaces can be automatically constructed by using the surface-growing method (SGM) (Wu and Hale, 2016). In this method, a fault surface is constructed to be a fault skin, which represents a link-data structure of fault samples (Figure 3a). Beginning with a fault sample that has a sufficiently high fault likelihood, a fault skin is produced by recursively searching and connecting the above, below, left, and right fault samples within a local seismic sampling grid. Such a fault skin is increasingly growing until there are no more neighboring fault samples (with similar fault attributes) to be linked. The resulting fault skin often consists of the consistently aligned and linked fault samples, which represent a locally planar surface. Thus, the fault skin can appear to be a piecewise constant approximation of a fault plane by enlarging the size of each fault sample (Figure 3b). Figure 3c shows every fault plane or surface constructed using SGM.

However, by directly linking the nearby fault samples, the constructed fault surfaces usually suffer from holes (highlighted by the arrows in Figure 3c). The noise level in the seismic image is significantly responsible for the holes appearing on the surfaces. The data noise not only blurs the obtained fault attributes but also introduces spurious fault samples, such that SGM may not be able to look for related fault samples to link and form complete fault planes. In addition, this method assumes that the faults are locally planar. That means that, by using SGM, only the nearby fault samples are connected to a fault skin and approximate a fault surface. This definition, however, is not necessarily real for some complicated faults with rapidly varying orientations or complex spatial shapes, such as the conical fault, which cannot be exactly approximated by the locally planar surfaces. Because it is hardly possible to align all of the fault samples within a local sampling grid, SGM often suffers from missing fault samples in constructing those complicated faults. Furthermore, fault surfaces are typically irregular surfaces and are not located on a regular sampling grid, such that we actually do not know the position of the surface before we construct it. This poses challenges to fill the missing holes by using a regular interpolation method (e.g., nearest neighbors) because we do not know where to interpolate before we construct the surface.

Constructing crossing fault surfaces is still challenging for most existing fault surface interpretation methods other than for holes. Near the fault intersections, the fault geometry is highly complicated and the fault features are not clear in a seismic image, which often yields missing fault samples. In addition, the fault attribute computation is based on the assumption that each sample corresponds to only one fault, which is obviously incorrect for intersecting faults. Like most fault surface construction methods, SGM often produces holes in constructing fault surfaces near intersections.

The extracted incomplete fault surfaces with holes or missing samples cause difficulties in either estimating fault slips (Hale, 2013; Wu and Hale, 2016) or building structural models (Caumon

et al., 2009) because near holes it is difficult to determine which seismic reflectors should be correlated. In the next sections, we propose two inversion-based approaches to robustly construct more complete fault surfaces in the presence of noisy or missing fault samples. In contrast, we consider SGM as the reference method.

Inversion-based methods

Constructing fault surfaces from oriented fault samples is similar to the surface reconstruction problem (Alexa et al., 2003; Kazhdan et al., 2006; Guennebaud and Gross, 2007) that has considerably progressed in the computer vision and computer graphics fields. Inspired by those methods developed for numerous computer vision tasks, we propose two inversion-based methods to construct fault surfaces. Instead of constructing the link-data structure of nearby fault samples, we estimate a spatially continuous scalar function throughout the whole image space to indicate fault surfaces by solving an optimization problem. First, without any assumption of the locally planar surface approximation, the fault surfaces extracted from the scalar function can be more complete, capable of constructing any complicated fault surface topology. Second, this implicit scalar function can be transformed into any data-structure format to flexibly represent fault surfaces with high resolution. Third, by formulating an inverse problem, we can introduce additional constraints into the proposed methods to more robustly deal with the noisy fault samples.

In both of the proposed methods, a basic step is to construct fault samples from fault attributes before the next fault surface construction. Besides, we follow SGM to exclude possibly spurious fault samples that usually have inconsistent orientations within a local sampling grid. This can be implemented by setting an appropriate threshold beforehand, including the number of linked samples and the tolerance of attribute similarity. This operation is also computationally lightweight and imposes only a slight increase in the computational burden. We take the preserved fault samples as the input of the proposed methods (Figure 2e).

Poisson equation surface method

Motivated by the success of surface reconstruction in computer graphics and computer vision (Kazhdan et al., 2006; Kazhdan and Hoppe, 2013), we propose the Poisson equation surface method (PESM) to construct fault surfaces from oriented fault samples scanned from a seismic image. In PESM, we solve the weighted Poisson equation for an implicit scalar function whose gradient best fits the orientations of the fault samples in the least-squares sense weighted by fault likelihood. The fault surfaces are implicitly represented by isosurfaces of this calculated scalar function. For this reason, the fault samples sparsely distributed in the seismic image are interpolated to form a spatially continuous fault normal vector field before they are fed into the next calculation. This vector field provides precisely enough information about the first derivatives of the implicit scalar function. Therefore, the fault surface construction is cast as how to find an integral relationship between this vector field and an unknown scalar function. We solve a partial differential equation to estimate the scalar function and then infer fault surfaces from it:

$$\nabla\chi = \mathbf{V}, \tag{1}$$

where χ represents an unknown scalar function and $\mathbf{V}$ denotes the fault normal vector field constructed from the fault samples and their corresponding orientations. This equation provides an orientation constraint to infer the shapes of the fault surfaces implicitly described by the scalar function. However, the positions of the fault surfaces are still unknown. The problem remains in finding an appropriate value of isosurfaces that can best approximate the target fault surfaces. By matching the orientation constraint alone, one may first globally shift (subtract) the scalar function by the average of the scalar values at the fault samples and then extract the zero isosurfaces of the shifted scalar function as the fault surfaces. However, it might be difficult to find a proper global shift because the scalar function is often locally drifted from the fault surfaces due to noise.

To seek an optimum value of isosurfaces from the scalar function, we impose an extra position constraint to encourage the constructed surfaces to pass through most of the input fault samples. Specifically, the position constraint is similar to a regularization that penalizes the deviation of the scalar function from zeros at fault samples. Thus, the whole inversion can be less prone to oscillations and less sensitive to outliers in solving for the scalar function.

In addition, each fault sample provides a confidence level described by its fault likelihood. Taking advantage of this attribute, we weight the vector field and the scalar function with the fault likelihood so that the fault samples with high likelihood values are significant in calculating the scalar function. By simultaneously minimizing the orientation and position constraint terms weighted by the fault likelihoods, we formulate the objective function as follows:

$$\begin{bmatrix} \mathbf{W}\nabla\chi \\ \mu\mathbf{W}\tilde{I}\chi \end{bmatrix} \approx \begin{bmatrix} \mathbf{WV} \\ \mathbf{0} \end{bmatrix}, \tag{2}$$

where μ denotes a constant coefficient that balances the importance between the two terms; we set μ to one for all examples in this study. The term $\tilde{I}$ represents a diagonal matrix with ones at the fault samples with zeros elsewhere. By solving these equations, we compute a spatially continuous scalar function whose gradient best matches the vector field $\mathbf{V}$ and zero isosurface mostly passes through the fault samples.

However, an explicit solution of a scalar function is not available from the equation above because the vector field $\mathbf{V}$ may generally not be integrable and the geometry of the fault surfaces is unknown. Still, we expect to find an approximate solution of an unknown scalar function in a weighted least-squares sense by solving the corresponding normal equation as follows:

$$(\nabla^{\mathrm{T}}\mathbf{W}^2\nabla + \mu\tilde{I}\mathbf{W}^2)\chi = \mathbf{W}^2\nabla^{\mathrm{T}}\mathbf{V}. \tag{3}$$

If we ignore the position constraint, this normal equation is a naive Poisson equation. Thus, we in fact solve for a scalar function whose Laplace term approximately equals the gradient of the vector field while satisfying the position constraint condition.

This linear equation is solved by the conjugate gradient method (Shewchuk, 1994), where we avoid explicitly forming large matrices for a problem in spatial dimensions. Figure 4a shows a scalar function computed from the oriented fault samples (Figure 2e) by solving equation 3. In this computed scalar function (Figure 4a), the

red color represents positive values, the blue color represents negative values, and the white color indicates values close to zero.

When we have obtained a scalar function, the next step is to extract fault surfaces represented by zero isosurfaces of this scalar function. The fault surfaces (Figure 4b) can be interpreted by extracting the zero isosurfaces. By using the marching cubes method, we construct the fault surfaces into triangle mesh structures, noting that more data structures could be used here as well. In fact, the scalar function can be conveniently transformed into any format to flexibly represent fault surfaces. Figure 4c displays that every fault surface provided by PESM is more complete relative to those shown in Figure 3c.

Point-set surface method

In addition to PESM, we propose the point-set surface method (PSSM) to construct fault surfaces. The method is based on local moving least-squares fitting for algebraic spheres (Guennebaud and Gross, 2007; Guennebaud et al., 2008), which demonstrably reconstructs surfaces from point-set data. With oriented fault samples as the input, the method can provide a reliable estimation of the mean curvature of the surface, allowing for robust handling of sharp features and boundaries.

To clearly demonstrate the problem, we first define the position of an arbitrary image point $\mathbf{x} = [x_1, x_2, x_3]^{\mathrm{T}}$ in a seismic image. As discussed previously, we take the fault samples equipped with orientations and fault likelihoods as the input to construct fault surfaces. In PSSM, we first compute an algebraic spherical coefficients $\mathbf{u}(\mathbf{x}) = [u_0, \ldots, u_4]^{\mathrm{T}} \in \mathbf{R}^5$ at each image point $\mathbf{x}$ by locally matching the oriented fault samples in the least-squares sense. This is because fitting a high-order algebraic sphere (Pratt, 1987) rather than a geometric sphere can improve the stability if a fault surface can be well approximated by a plane. With an algebraic spherical coefficient vector $\mathbf{u}(\mathbf{x})$, we can derive an algebraic sphere

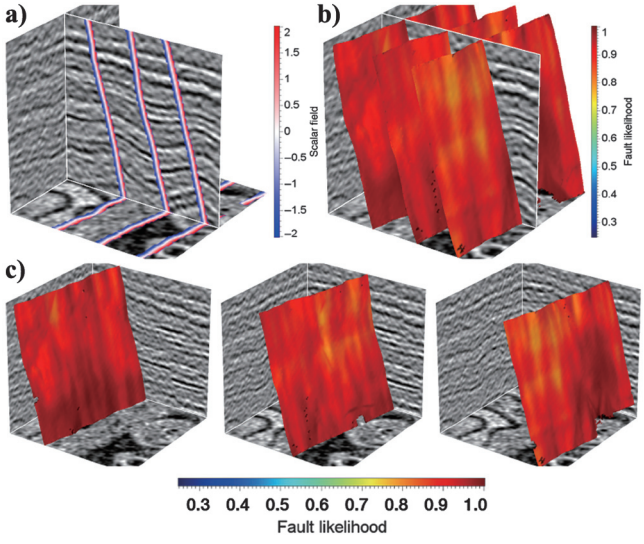

Figure 4. Fault surface construction using PESM. In this method, an implicit fault scalar function (a) is first estimated from the oriented fault samples (Figure 2e). The fault surfaces are then constructed by extracting the zero isosurfaces from this scalar function. In this way, the fault surfaces (c) are less sensitive to noise and more complete than those of SGM shown in Figure 3c.

$s_{\mathbf{u}(\mathbf{x})}(\mathbf{x}) = [1, x^{\mathrm{T}}, x^{\mathrm{T}}x]u(\mathbf{x})$. This formulation defines an algebraic distance between each image point $\mathbf{x}$ and the locally fitted spherical surface that matches the fault samples within its neighborhood. The fault surfaces are approximated by the surfaces of those algebraic spheres. Therefore, we can calculate the implicit scalar function $f(\mathbf{x})$ at image point $\mathbf{x}$ according to its algebraic distance:

$$f(\mathbf{x}) = s_{\mathbf{u}(\mathbf{x})}(\mathbf{x}) = [1, \mathbf{x}^{\mathrm{T}}, \mathbf{x}^{\mathrm{T}}\mathbf{x}]\mathbf{u}(\mathbf{x}). \tag{4}$$

The scalar function depicted by the algebraic distances has zero values only for the image points that are just located on the locally matched spherical surfaces. This means that the fault surfaces can be constructed by extracting the zero isosurfaces of this scalar function.

Instead of directly estimating a scalar function in PESM, the most significant difference in PSSM is deriving the algebraic spherical coefficients that represent an algebraic sphere at each image point. A moving least-squares method is exploited to fit the algebraic sphere whose surface best agrees with the neighboring fault samples within a search window $h(\mathbf{x})$ centered at each image point $\mathbf{x}$. The fault samples near this point can be efficiently found by using the k-dimensional tree method (Ramasubramanian and Paliwal, 1992). We use at least 20 fault samples in estimating an algebraic sphere. This means that the search window $h(\mathbf{x})$ varies with respect to point $\mathbf{x}$ to guarantee a sufficient number of fault samples considered in computing spherical coefficients. A few fault samples may overemphasize the local orientation features of faults while ignoring the global trends of the surfaces, making the method less robust to noise. However, using more samples may stabilize the calculation, but it smears detailed structural features of faults. Both cases lead to degraded accuracy of the resulting scalar function. Thus, an appropriate number of fault samples needs to be carefully selected based on a balance of local and global orientation features of fault surfaces. According to multiple experiments, we find that the PSSM result is relatively accurate when using 20 fault samples to estimate the algebraic spherical coefficients and further improvement introduced by parameter selection is not significant. Also, we set a maximum range of the search window up to 20 to exclude the fault samples far away from the image point at which we estimate the spherical coefficients.

In addition, the fault samples may have different contributions in fitting an algebraic sphere at the image point. The weighting of each fault sample is determined by not only its confidence level indicated by the fault likelihood, but also by its distance away from that image point, such that nearby fault samples with a higher fault likelihood are more significant in the calculation. Therefore, the approximation degree of the fault samples can easily be controlled, making PSSM well suited to suppress possible noise or suspicious fault features.

Let the $\mathbf{p}_i$ and $\mathbf{n}_i$ vectors denote the position and normal orientation of this i_{th} fault sample in the neighborhood of image point $\mathbf{x}$, respectively. We design a joint weighting scheme $w_i(\mathbf{x})$ for the ith fault sample as

$$w_i(\mathbf{x}) = \mathcal{F}(\mathbf{p}_i)\mathcal{D}\left(0\frac{\|\mathbf{p}_i - \mathbf{x}\|}{h(\mathbf{x})}\right), \tag{5}$$

where $\mathcal{F}$ represents the fault likelihood weighting term and $\mathcal{D}$ represents a distance weighting term that is defined as a compactly supported polynomial function:

DOI:10.1190/geo2019-0832.1

$$\mathcal{D}(x) = \begin{cases} (1-x^2)^4 & x < 1 \\ 0 & x \geq 1 \end{cases}. \tag{6}$$

To balance the magnitude of the two weighting schemes, the distance $\|\mathbf{p}_i - \mathbf{x}\|$ between the neighboring fault sample and the image point is required to be normalized with the search window $h(\mathbf{x})$. The choice of the fourth power is somewhat arbitrary, and it aims to increase the contrast among fault samples and this image point. The search window $h(\mathbf{x})$ is determined by the region in which we can find sufficient fault samples to estimate a local algebraic sphere as well as a given maximum size (20 samples). The spherical coefficient vector $\mathbf{u}(\mathbf{x})$ can be approximated in the least-squares sense. For each fault sample in the neighborhood of the image point $\mathbf{x}$, we minimize the algebraic distance $s_{\mathbf{u}(\mathbf{x})}(\mathbf{p}_i)$ of the fault sample position $\mathbf{p}_i$ and the deviation between the fault sample normal direction $\mathbf{n}_i$ and the gradient of algebraic sphere $\nabla s_{\mathbf{u}(\mathbf{x})}(\mathbf{p}_i)$. Thus, the objective function in PSSM can be formulated as follows:

$$\mathbf{u}(\mathbf{x}) = \arg\min_{\mathbf{u}} \sum_i w_i(\mathbf{x})(s_{\mathbf{u}(\mathbf{x})}(\mathbf{p}_i)^2 + \|\nabla s_{\mathbf{u}(\mathbf{x})}(\mathbf{p}_i) - \mathbf{n}_i\|^2). \tag{7}$$

The gradient of algebraic sphere $\nabla s_{\mathbf{u}(\mathbf{x})}(\mathbf{p}_i)$ describes its surface normal direction at fault sample position $\mathbf{p}_i$. Similar to PESM, this objective function is also composed of the position and orientation constraint schemes corresponding to the algebraic distance and the normal direction difference, respectively. However, we do not minimize the two constraint terms at the same time as PSSM. Instead, we first minimize the orientation constraint to infer the normals of the locally fitted spherical surfaces. Subsequently, we use the position constraint to specify the zero isosurfaces of the scalar function as the constructed fault surfaces. By separately minimizing two constraint terms, we can obtain an explicit solution of the coefficient vector $\mathbf{u}(\mathbf{x})$ that completely represents an algebraic sphere $s_{\mathbf{u}(\mathbf{x})}(\mathbf{x})$ with four coefficients (Guennebaud et al., 2008):

$$\begin{cases} u_0 = -[u_1 u_2 u_3] \sum \tilde{w}_i \mathbf{p}_i - u_4 \sum \tilde{w}_i \mathbf{p}_i^{\mathrm{T}} \mathbf{p}_i \\ \begin{bmatrix} u_1 \\ u_2 \\ u_3 \end{bmatrix} = \sum \tilde{w}_i n_i - 2u_4 \sum \tilde{w}_i p_i \\ u_4 = \frac{1}{2} \dfrac{\sum w_i p_i^{\mathrm{T}} n_i - \sum \tilde{w}_i p_i^{\mathrm{T}} \sum w_i n_i}{\sum w_i p_i^{\mathrm{T}} p_i - \sum \tilde{w}_i p_i^{\mathrm{T}} \sum w_i p_i}, \end{cases} \tag{8}$$

where $w_i = w_i(\mathbf{x})$ is defined in equation 5 and $\tilde{w}_i = w_i / \sum_j w_j$ is a normalized weight. Using these explicit formulations, we can efficiently solve the algebraic sphere coefficients everywhere in a seismic image because we can effectively avoid directly handling any large linear equation for a problem in spatial dimensions. Then, the scalar function can be derived by substituting the sphere coefficient vectors $\mathbf{u}(\mathbf{x})$ into equation 4. Figure 5a shows a scalar function obtained from the fault samples and their corresponding orientations (Figure 2e) by solving the corresponding equations 4 and 8. In the computed scalar function, the red color represents positive values, the blue color represents negative values, and the white color implies values close to zero. We finally construct a set of complete fault surfaces (Figure 5b) by extracting zero isosurfaces from this scalar function using the marching cubes method. Further details of every fault surface shown in Figure 5c demonstrate that PSSM can robustly construct fault surfaces from a noisy seismic image.

Noise level examples

The main error of our methods is introduced by the definition of the fault likelihood and the quality and uncertainty of the obtained fault likelihood and the orientation attributes. To verify the robustness of our methods against noise, we additionally design the four examples with varying noise-to-signal ratios (N/S), including 0.2, 0.4, 0.6, and 0.8 (from the left side to the right side in Figure 6a), respectively. Besides that, a quantitative measurement is used to compare the performance of the surface construction methods discussed in this study. We use the Hausdorff distance to evaluate the similarity between the real fault planes and the extracted surfaces. The Hausdorff distance is a mathematical construct used to measure the difference of two sets of points that are subsets of a metric space. Informally, we consider that two sets of points are close in the Hausdorff distance if every point of either set is close to some point of the other set. We define the Hausdorff distances $\mathcal{D}$ between the real fault planes X and the constructed surfaces Y as follows:

$$\mathcal{D} = \max(\sup_{x \in X} \inf_{y \in Y} \mathcal{D}(x, y), \sup_{y \in Y} \inf_{x \in X} \mathcal{D}(x, y)), \tag{9}$$

where $x \in X$ and $y \in Y$ are the elements within X and Y, respectively, and $\mathcal{D}(x, y)$ represents the Euclid distance between the x and y elements. In addition, sup is the supremum function, whereas inf is the infimum function. We show the fault surfaces constructed by using the reference method (Figure 6b), PESM (Figure 6c), and PSSM (Figure 6d), respectively. In the cases of mild noise (0.2), we can observe that the three methods provide comparable performance. However, when the N/S increases to 0.4, the reference method (SGM) starts suffering from locally missing samples (denoted by the arrows in Figure 6b), whereas PESM and PSSM perform well for accurately constructing fault surfaces without holes. The result of the reference method becomes even worse in a stronger noise case

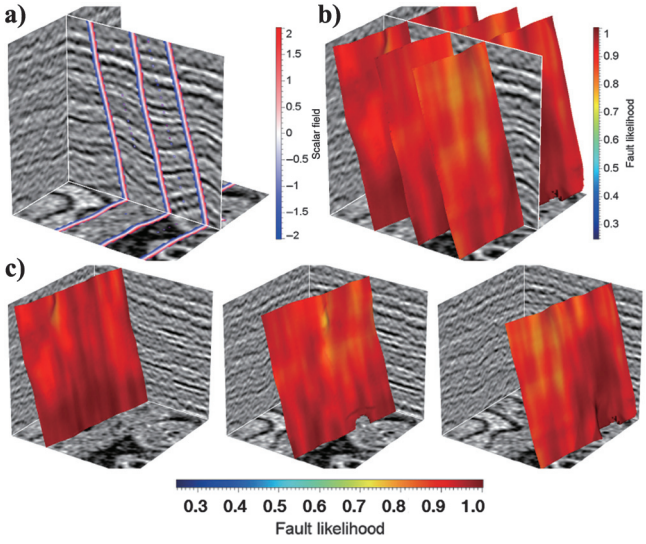

Figure 5. Fault surface construction using PSSM. In this approach, we use a moving least-squares spherical fitting fashion to compute (a) a global scalar function whose zero isosurfaces best represent the (b) fault surfaces. Like PESM (Figure 4), PSSM can robustly construct comparable fault surfaces without any holes (c) from a noisy seismic image as well.

DOI:10.1190/geo2019-0832.1

(0.6 and 0.8). In contrast, the PESM and PSSM methods still provide reliable solutions with sufficient accuracy.

More details are revealed by measuring the Hausdorff distances between the actual fault planes and the constructed fault surfaces. According to Table 2, we can find a solution consistent with our previous observations. In all four noise level examples, the proposed methods both provide results with smaller Hausdorff distances. This means that they have a better similarity to the real fault planes. Thus, we claim that the proposed methods are more resilient to noise in contrast to the reference method. Furthermore, we also observe that PESM is more robust than PSSM when they are implemented to construct fault surfaces from a highly noisy seismic image (larger than 0.6).

FAULT SAMPLE CLASSIFICATION

PESM and PSSM have shown great promise in constructing complete fault surfaces in the previous synthetic examples. However, the challenge still remains in constructing crossing faults. To clearly demonstrate that, we design another synthetic seismic image with crossing faults. Following the same procedure previously discussed, we first scan the seismic image and search for the maximum fault likelihood while recording the corresponding orientation (strike and dip) everywhere to compute three fault attributes. Then, we construct fault samples at the ridges of the fault likelihood (Figure 7a) and we further filter those spurious samples unrelated to faults using SGM. With the preserved oriented fault samples as the input (Figure 7b), we can further construct fault surfaces using the proposed methods.

From the solutions provided by PESM (Figure 7c) and PSSM (Figure 7d), however, one can observe some spurious distortions or discontinuities appearing on the faults near the intersections (highlighted by the arrows in Figure 7c and 7d). Those anomalous features are certainly not shown in a ground truth of the fault planes. Because multiple fault orientations exist near the intersection, a

Table 2. The Hausdorff distances between the actual fault planes and constructed surfaces in the noise-level examples.

N/S	SGM	PESM	PSSM
0.2	5.4535	2.1474	0.7770
0.4	10.2094	4.6075	4.5655
0.6	17.8554	5.0850	7.6178
0.8	24.7148	12.1851	15.7320

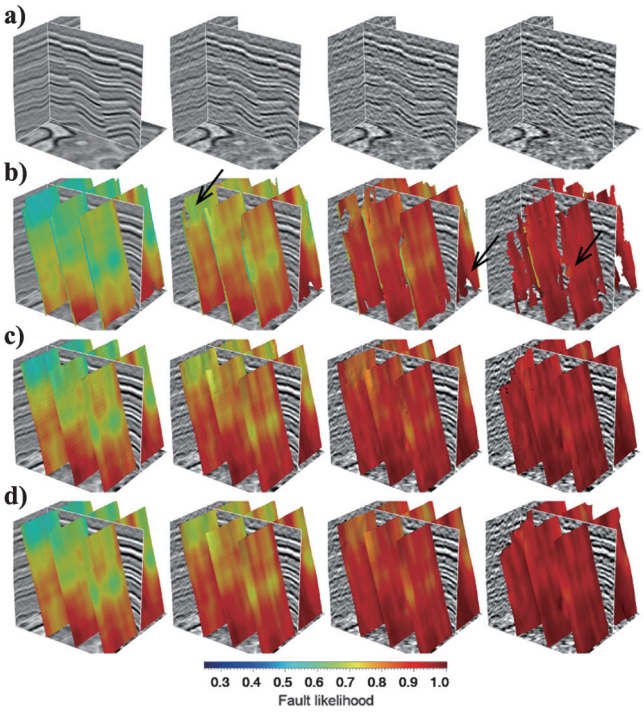

Figure 6. Numerical examples for varying levels of noise in seismic images. To verify the robustness of our methods, we show four examples with increasing N/Ss of 0.2, 0.4, 0.6, and 0.8 (from the left side to the right side in [a]). In cases of mild noise (0.2), the three methods provide comparable performance. However, when the N/S increases to 0.4, the reference method starts suffering from locally missing samples (highlighted by the arrows), whereas PESM and PSSM can construct the complete fault surfaces. The result of the reference method becomes even worse in a stronger noise case (0.6 and 0.8). In comparison, PESM and PSSM still provide fault surfaces without any holes.

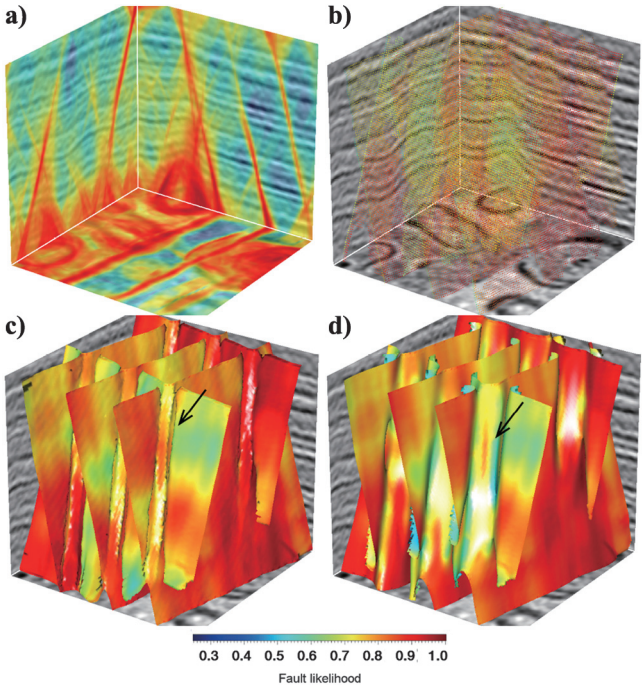

Figure 7. Another example of a synthetic seismic image with multiple crossing faults. (a) The fault likelihood image is calculated by using the fault scanning method. (b) The fault samples, extracted at the ridges of the fault likelihoods, are used in PESM and PSSM to construct fault surfaces in (c and d), respectively. But we find that the surfaces complicatedly intersect with each other near the fault intersections (highlighted by arrows). That means the challenge still remains in constructing the cross-fault surfaces. Significant distortions are observed in the intersecting areas of the surfaces constructed by the (c) PESM and (d) PSSM methods, which indicates that both the methods fail to reasonably construct intersecting fault surfaces.

DOI:10.1190/geo2019-0832.1

single value of isosurfaces cannot well approximate those almost orthogonally oriented fault samples. To solve this problem, we propose to group the fault samples according to their orientations before they are fed into the fault surface construction. In this way, we can independently construct consistently oriented surfaces without crossing faults from a group of fault samples. The final solution is obtained by merging the fault surfaces constructed in every single group.

Without any preliminary information as required for choosing the class number, we use a nonparametric method called density-based spatial clustering of application of noise (DBSCAN) (Ester, 1996) to automatically find groups (classes) of fault samples. This algorithm is performed with the employment of the scikit-learn (Pedregosa et al., 2011) repository. As mentioned above, the fault skin is actually a set of linked fault samples with locally similar attributes. When performing the DBSCAN, we consider the fault samples within each fault skin as a classification unit instead of a single fault sample. By taking advantage of its linking data structure, we avoid classifying those locally aligned fault samples in a fault skin because they might be located on the same fault. Additionally, since the number of the fault skins is typically less than the fault samples, this significantly improves the computational efficiency as well as easing the computational burden. Before fault sample classification, we need to reasonably describe the orientation features for the samples in a fault skin.

Fault orientation feature

To reasonably represent the orientation features for the fault samples within a fault skin (the first row in Figure 8), we define an orientation feature tensor that consists of two orientation components including strike and dip, respectively (the last two rows in Figure 8). In an orientation feature tensor, the strike or dip component is represented as a 4×4 matrix with 16 elements. Each element in the matrix describes a local strike or dip feature spatially associated with one patch in the fault skin, and the local orientation feature is computed as the weighted average (weighted by the fault likelihoods) of strike or dip angles for all of the fault samples on this patch of fault skin.

To construct such orientation feature tensor, the fault samples in a fault skin need to be divided into 16 parts to compute the corresponding 16 local orientation (strike or dip) features in the matrix. Specifically, we first search for a central fault sample with the minimum distance along its normal (determined by strike and dip angles) from the center point on this fault skin. We then define two auxiliary planes that pass through the central fault sample, and their normals coincide with the strike and dip, respectively, to divide the fault skin into four parts. By recursively subdividing these four parts, we obtain 16 smaller segments. We estimate a weighted average of strike and dip, respectively, for each segment of the fault skin.

Therefore, the strike or dip component in the orientation feature tensor is represented by a matrix with 16 local orientation features. Each orientation feature tensor is composed of two such matrices of the strike and dip components to represent a spatial orientation feature of the fault skin. Because the clustering method is sensitive to the scaling of the input data, we normalize each element in the tensor such that the local orientation feature falls between 0 and 1. The second and third rows of Figure 8 show the strike and dip components with normalized strike and dip angles. As shown in Figure 8, we can observe that the defined strike components of fault skins 1, 2, and 4 are nearly blue whereas the strike components for the other skins are nearly red. The defined dip components of fault skins 1, 2, and 4 are nearly white, whereas the dip components for the other skins are nearly black. This means that the strike and dip components of the defined orientation feature tensor can be used to effectively separate the two sets of intersecting fault skins into two different clusters.

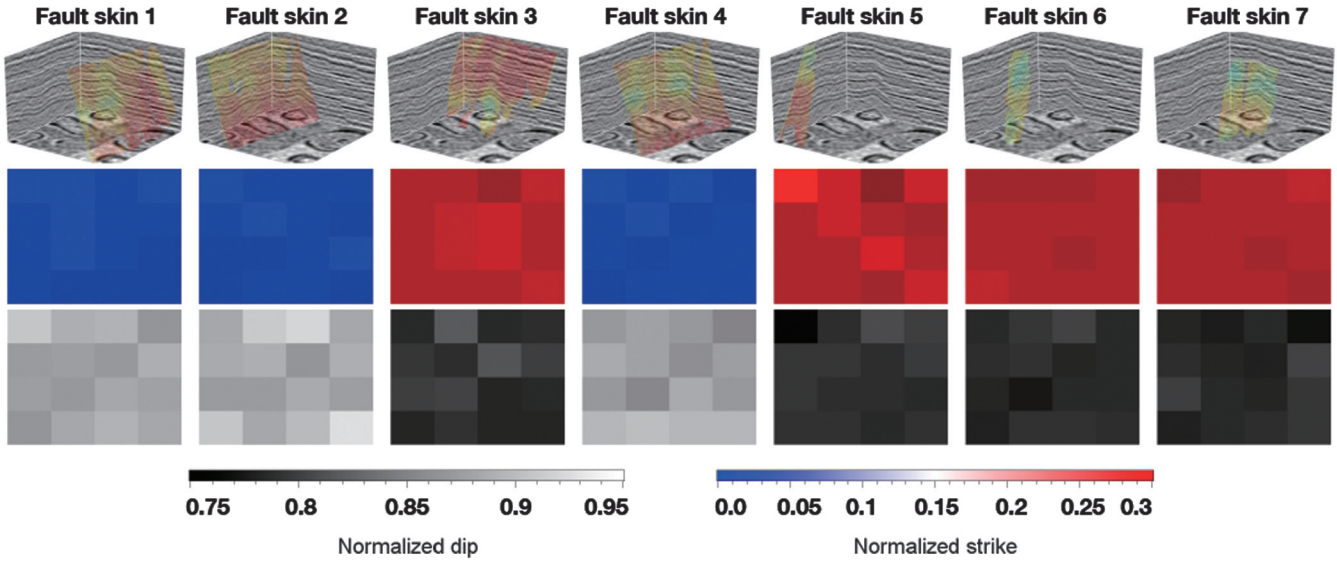

Figure 8. An example of fault sample classification. To appropriately deal with the crossing faults, we first link locally well-aligned fault samples to construct fault skins. The fault skin is a set of linked fault samples which represent only a local fault segment (e.g., the right three skins). We then compute an oriented tensor to characterize the spatially varying orientations of each fault skin. Such an oriented tensor consists of the strike (second row) and dip (third row) components, and each one is a 4×4 matrix with 16 elements. The element in the matrix represents an orientation feature locally associated with the related fault segment. These fault skins (the fault sample sets) are further grouped into multiple classes according to the correspondingly oriented tensor.

DOI:10.1190/geo2019-0832.1

Density-based clustering

We use DBSCAN to classify the fault samples shown in Figure 7b. This method has proven its ability in grouping data according to their similarity and discovering clusters with arbitrary shapes (Ester, 1996; Zhou et al., 2000). In contrast to some clustering algorithms, it does not require the predetermination of the class number. DBSCAN only takes the two parameters of *eps* and *minpts* to define a cluster as a region of dense fault samples separated by regions of relatively sparse fault samples. Specifically, *eps* specifies the maximum orientation variation of samples allowed in a cluster and *minpts* denotes the minimum number of samples as required to form this cluster. To incorporate all of the fault skins and make their orientation features sufficiently similar within a cluster, we set the *eps* and *minpts* equal to 0.2 and 1.0, respectively, for all of the data examples in this study. By using DBSCAN, the seven fault skins displayed in Figure 9a are automatically grouped into two classes (clusters), and we exhibit each fault sample group in Figure 9a and 9b, respectively.

Then, we take the groups of fault samples as input to repeatedly perform PESM and PSSM. In each run of the calculation, we typically obtain a set of oriented fault surfaces. We again observe that the fault surfaces obtained from PESM (Figure 10a) and PSSM (Figure 10b) are more complete and continuous than the reference method (Figure 10c). More importantly, in comparison to the direct solutions of PESM (Figure 9e) and PSSM (Figure 9f) without classification, we find that the fault surfaces have been successfully constructed from fault samples even in fault intersections in which spurious distortions have been successfully eliminated. Due to the limitation inherent in the scanning method (only one fault sample per seismic sample), the fault samples are often locally missing around the fault intersections. We observe that the holes (highlighted by the arrows) appear on the constructed surfaces in the reference method. In this case, the proposed methods can reasonably fill holes or missing samples and construct complete surfaces.

Constructing faults with complex shapes

The proposed methods are not limited to planar faults and can be used to successfully construct any complicatedly curved or bended fault surfaces. To demonstrate that, we further provide a synthetic example with a highly curved conical fault that has all strike angles ranging from 0° to 360°. This new seismic volume (Figure 11a) contains a conical fault and two small planar faults that do not all cross the entire image space. Following the same procedure discussed above, we estimate a fault likelihood image as well as the orientation images (strike and dip), and then we construct the fault samples. With SGM, those samples are grouped into fault skins by measuring the local attribute similarity. According to their orientation features, the fault sample groups can be further automatically classified into two sets corresponding to the conical fault (Figure 11c) and the two small planar faults (Figure 11d), respectively. In constructing such a conical fault, classifying a single fault sample might separate the samples that might be on the same fault. This is the other reason why we choose to classify the fault skin rather than each single fault sample. By using the proposed methods, we take the two groups of fault samples as input to compute the corresponding scalar functions and further extract fault surfaces. The final solutions of both methods can be obtained by merging all of the fault surfaces constructed from each group of fault samples.

We exhibit the fault surfaces obtained by using PESM in Figure 11e and PSSM in Figure 11f. In comparison to the reference method (Figure 11b), we again observe that our methods can work well to construct such a complex fault with a highly curved surface (the holes are indicated by the arrows in Figure 11b). For more de-

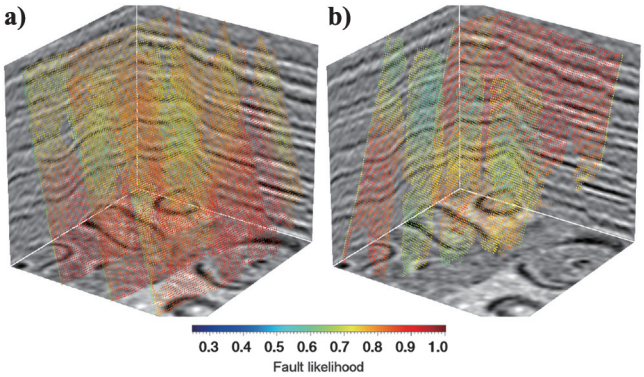

Figure 9. After the classification, we obtain two groups (clusters) of fault samples shown in (a and b). The fault samples in a single group are consistently oriented and are no longer crossed with each other, such that the corresponding fault surfaces can be correctly constructed without any distortions by using both of the proposed methods.

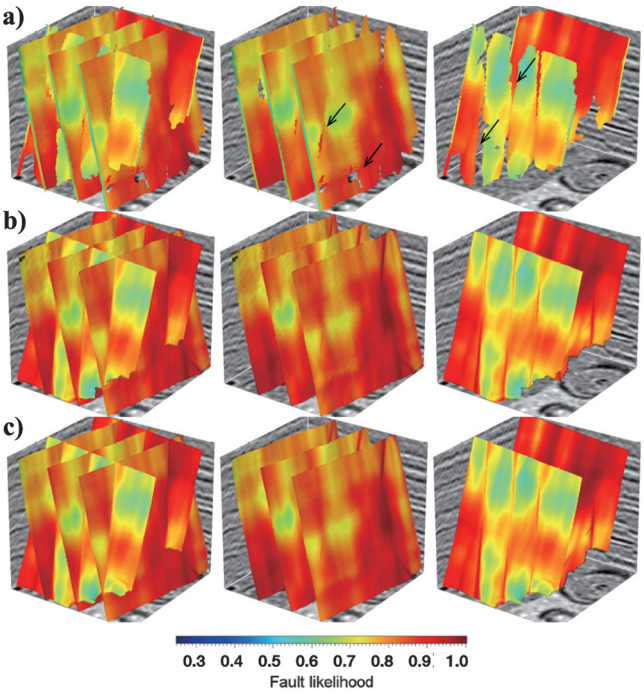

Figure 10. A comparison of the solutions provided by different fault surface construction methods. With the two independent groups of fault samples (Figure 9), the fault surfaces can be automatically constructed by (a) the reference method (SGM), (b) PESM, and (c) PSSM, respectively. Due to the definition of the fault likelihood (only one estimation per seismic sample), the fault samples are locally missing around the fault intersections. We can observe that the holes (highlighted by the arrows) appear on the constructed surfaces in the reference method. In this case, however, the proposed methods can reasonably fill holes or missing samples and construct complete surfaces.

DOI:10.1190/geo2019-0832.1

tails, we especially show the conical fault (Figure 11g and 11h) constructed from the corresponding fault samples (Figure 11c) by using PESM and PSSM, respectively. For both of our approaches, we have used a fault likelihood image as a quality map to weight the equations in solving the equations for constructing fault surfaces. All of the constructed fault surfaces are colored by the related fault likelihood values, such that we can evaluate the solution uncertainties. For example, the boundaries of two small planar fault surfaces can be clearly identified with low fault likelihood in Figure 11b, 11e, and 11f.

APPLICATIONS TO FIELD SEISMIC IMAGES

As shown in the workflow in Figure 12, our fault surface construction methods mainly consist of four steps: (1) compute the fault attributes, (2) construct the fault samples, (3) estimate the scalar function by PESM or PSSM, and (4) extract the fault surfaces. According to the synthetic examples above, our approaches successfully produce complete and continuous fault surfaces without any holes even at the fault intersections. We further apply PESM and PSSM to the two field seismic volumes.

Case study 1

Figure 13a shows a 3D subset (381 [inline] ×210 [crossline] ×450 depth samples) of a real seismic image complicated by crossing faults. From such an image, the fault likelihood, strike, and dip attributes are first simultaneously computed by scanning along all possible fault orientations. As shown in Figure 13b, the fault likelihood attributes highlight most of the faults in the seismic image. Then, we thin these fault attributes and construct fault samples at the ridges of the fault likelihood image. As shown in Figure 13c, the fault samples can be displayed as squares colored by the fault likelihoods and oriented by the related strike and dip angles. We further use SGM (Wu and Hale, 2016) to find 34 sets of fault samples locally aligned while filtering the spurious or noisy samples that cannot be linked to form significantly large surfaces. By using DBSCAN, we group the sets of fault samples into eight clusters (classes) according to their orientation features. To handle the complex crossing faults, we independently take each cluster of fault samples as an input to construct the surfaces.

Instead of representing fault surfaces by linked fault samples in the reference method, fault surface construction is implemented by solving a scalar function in both of the proposed methods. In PESM, we first create a spatially continuous fault normal vector field from the oriented fault samples, and then we solve a weighted Poisson equation with a least-squares method to derive a scalar function whose zero isosurfaces can best represent the fault surfaces. In PSSM, we solve an algebraic sphere coefficient vector at each image point to define an algebraic spherical surface that matches nearby fault samples around this point. The implicit scalar function is then computed as the algebraic distance from each image point to

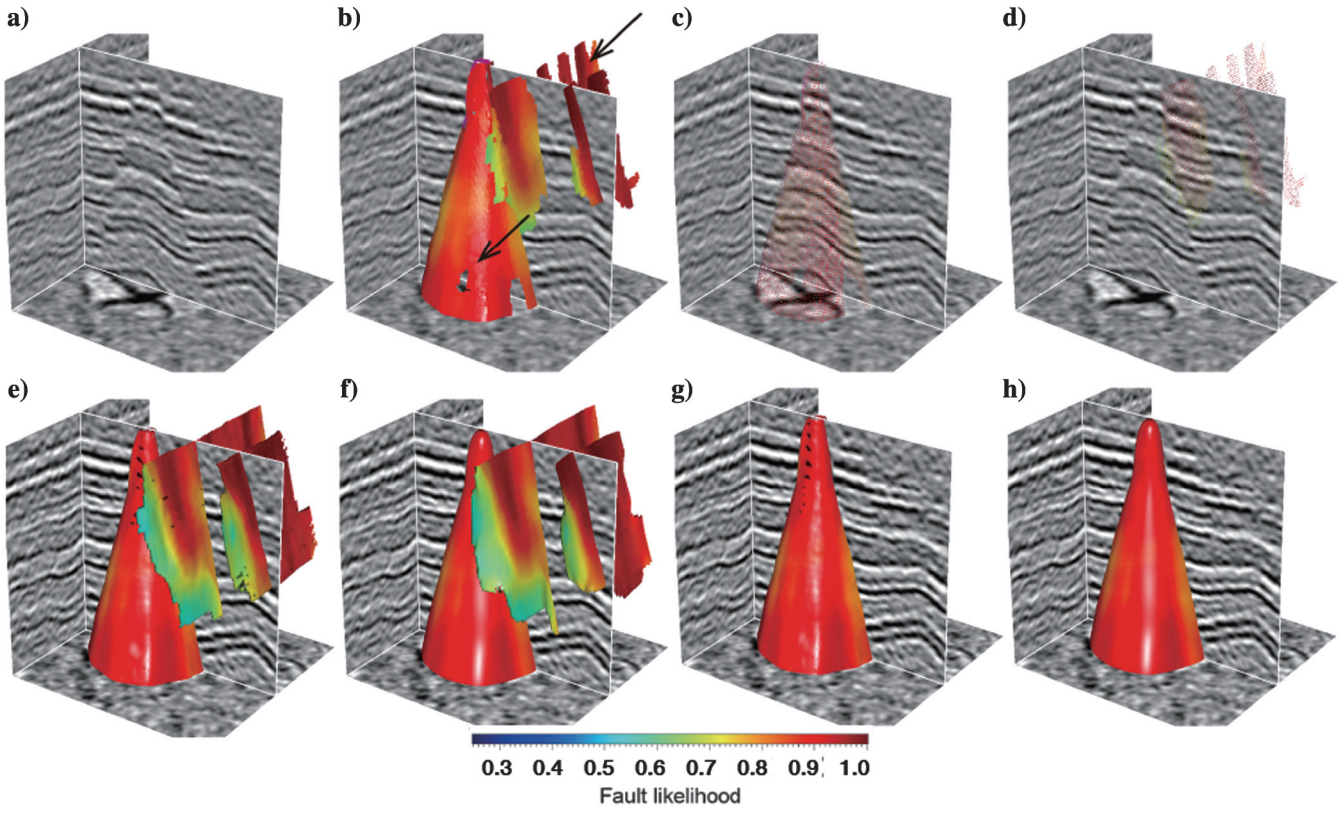

Figure 11. A more complex example of constructing curved fault surfaces. (a) The seismic volume contains a special conical fault and two small planar fault surfaces, which all do not cross the entire image domain. In this case, the scanned fault samples can be grouped into two sets according to their orientations shown in (c and d). In comparison to (b) the reference method, the fault surfaces obtained from (e) PESM and (f) PSSM further demonstrate that our method can work well to construct such complex faults with a special conical shape. The constructed conical faults using our PESM and PSSM are displayed in (g and h), respectively.

DOI:10.1190/geo2019-0832.1

the corresponding estimated spherical surface. For both of our approaches, the set of complete fault surfaces can be constructed by extracting zero isosurfaces from the scalar function by using the marching cubes method.

The fault surfaces constructed by the reference method, PESM, and PSSM are shown in Figure 13d–13f, respectively. In addition, we display the fault surfaces constructed from four major clusters of fault samples by using the three methods in Figure 14a–14c, respectively. We observe that a set of consistently oriented fault surfaces is constructed from each cluster of fault samples, which verifies a successful application for the fault sample classification. In comparison to the reference method, inversion-based approaches can recover more complete fault surfaces with fewer holes.

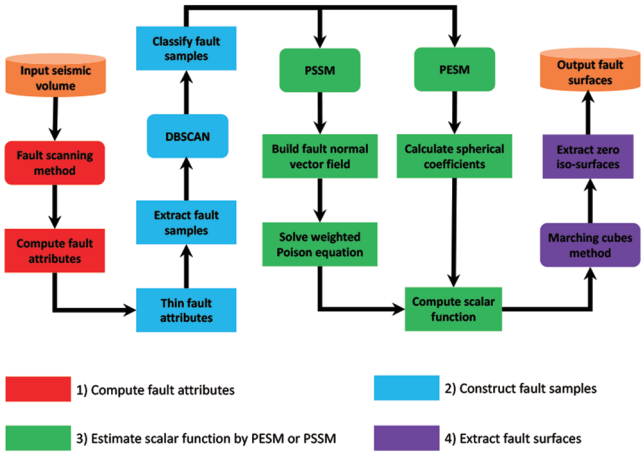

Figure 12. The workflow of our inversion-based methods mainly includes four steps: (1) compute fault attributes, (2) construct fault samples, (3) estimate scalar function by PESM or PSSM, and (4) extract fault surfaces.

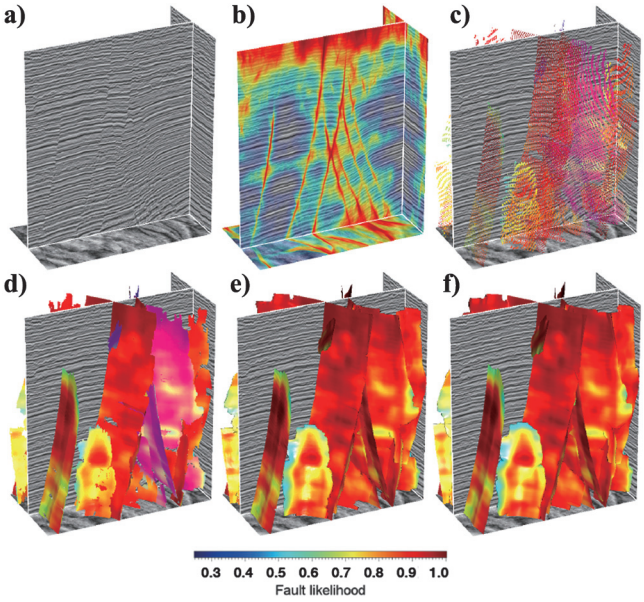

Figure 13. A case study of the proposed methods. In the first field seismic image (a), we scan for (b) a fault likelihood image, and then we construct (c) oriented fault samples. The fault samples are further clustered into different groups from which the fault surfaces are finally constructed by using (d) the reference method (SGM), (e) PESM, (f) PSSM, respectively.

Case study 2

To further demonstrate the effectiveness of our methods, we apply PESM and PSSM to another real 3D seismic image (287 [inline] ×735 [crossline] ×889 [time] samples) shown in Figure 15a. Following the same processing discussed above, we construct fault surfaces from fault samples. By using the fault scanning method, we derive a fault likelihood image (Figure 15b) while recording the corresponding orientations (not shown). With the attribute images of fault likelihood, strike, and dip, we construct the fault samples at the ridges of the fault likelihood. Although the fault likelihood image has detected most of the faults, however, we can observe that some discontinuities unrelated to faults are also highlighted. As discussed previously, we use SGM (Wu and Hale, 2016) to measure the attribute similarity nearby and then we exclude those fault samples unrelated to faults. In this way, we obtain 123 sets of fault samples (Figure 15c).

Figure 15d shows the fault surfaces constructed by linking the fault samples within each skin. However, the fault surfaces constructed by the reference method suffer from holes or locally missing samples. To overcome this problem, we use the proposed approaches to reasonably fill holes and robustly construct more complete fault surfaces. Specifically, we use DBSCAN to group the fault sample sets and then separately construct the fault surfaces by using PESM or PSSM. For this real data application, the fault samples (Figure 15c) are automatically grouped into 11 clusters. Considering the fault samples in each group as input, we compute a spatially continuous scalar function and then extract a triangulated approximation of fault surfaces by using the marching cubes method. Figure 15e and 15f, respectively, displays the fault surfaces constructed by PESM and PSSM, respectively. We again observe that the fault surfaces obtained by the

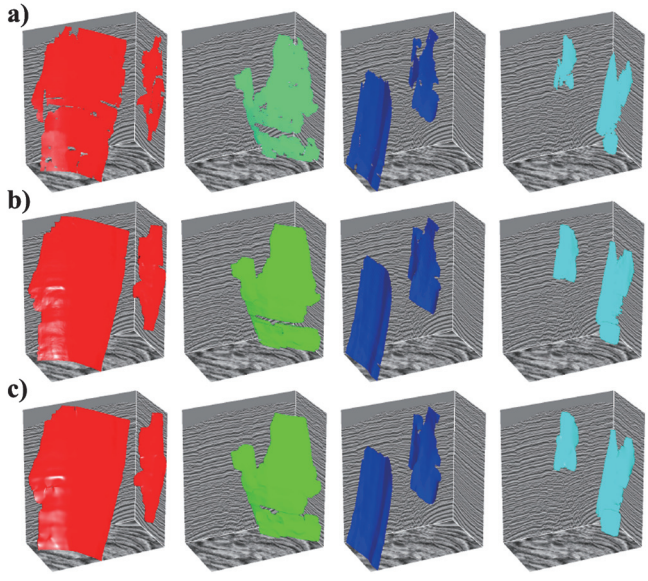

Figure 14. The fault surfaces constructed by the grouped fault samples. To show more details of the fault surfaces in Figure 13, we display the four fault surfaces that are separately constructed from the four groups of fault samples using (a) the reference method (SGM), (b) PESM, (c) and PSSM, respectively.

proposed approaches are more continuous and complete in contrast to the reference method (Figure 15d).

DISCUSSION

We apply our proposed methods on the four synthetic seismic images, where the noise levels are very different, to test their robustness against outliers. According to Table 2, the constructed fault surfaces have smaller Hausdorff distances than the reference method in all four numerical examples. This means that their solutions provide a better similarity to the real fault planes. Furthermore, we also observe that PESM outperforms PSSM in a highly noisy seismic image. However, because most computation time in the fault surface interpretation is consumed on estimating the scalar function, performing PSSM is more efficient than PESM that involves an iterative solver. Using a 28-core computer, our parallel implementation of PSSM takes approximately 136.5 s whereas PESM requires approximately 501.7 s for processing the first real seismic image. In the second field example with a larger data set, we observe that the efficiency improvement of PESM is even more significant. It takes 322.5 s with PSSM compared to 2711.5 s with PESM, which shows approximately a 90% run-time savings.

The accuracy of our methods depends on not only the definition of the fault likelihood, but also the quality and uncertainty of the obtained fault likelihood in addition to the orientation attributes. Thus, complex noise patterns and challenging stratigraphic features in the seismic image could degrade the quality of those attributes and subsequently degrade the fault surface construction. Besides, another difficulty lies in how to identify a single fault or multiple faults in constructing fault surfaces from fault samples within a local neighborhood smaller than the search region of the k-dimensional tree method. The search region is defined on the sampling grid of seismic image as well as related to the number of neighboring fault samples. This means that the sensitivity with respect to the distance between fault planes is also associated with data resolution.

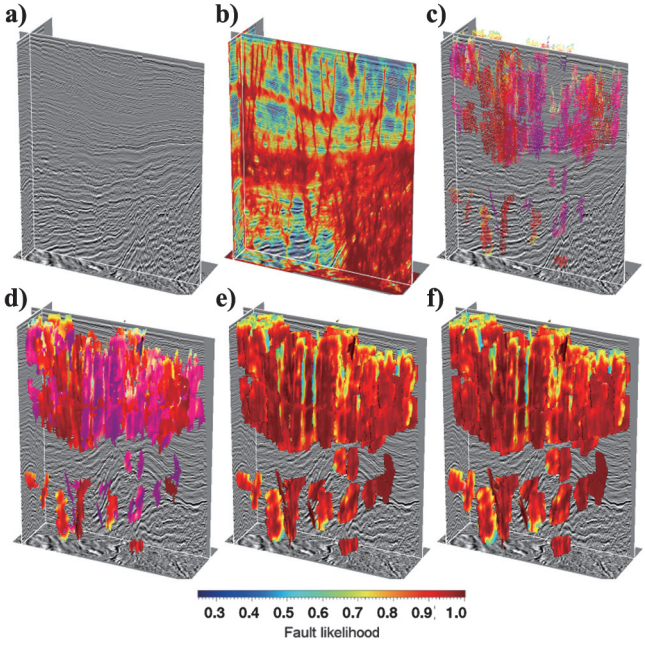

Figure 15. Another case study of the proposed methods. In the second field seismic image (a), we first compute (b) a fault likelihood image to highlight the fault positions as well as orientations, and then extract (c) fault samples at the ridges of the likelihoods and further filter those spurious samples. The fault surfaces are constructed by using (d) the reference method (SGM), (e) PESM, and (f) PSSM, respectively.

CONCLUSION

We have proposed two inversion-based approaches of PESM and PSSM to more robustly construct fault surfaces by inverting a spatially continuous scalar function from oriented fault samples. The complete fault surfaces can be efficiently extracted from an appropriate isosurface of the scalar function by using the marching cubes method. The scalar function can be transformed into any format of the data structure to efficiently and flexibly represent fault surfaces. For example, in this study, we extract a triangulated approximation of fault surfaces as individual triangle-mesh items, which can be selected or excluded for the requirement of the following geologic modeling or fault slip estimation.

In PESM, we expect to find a scalar function whose gradient matches a fault normal vector field constructed from the oriented fault samples. The key insight of this method is to find an integral relationship between the vector field and the scalar function. In a least-squares sense, estimating the scalar function from the fault normal vector field is cast as solving a weighted Poisson equation. To avoid explicitly forming large matrices for the 3D fault surface interpretation problem, we iteratively solve the equation to derive the scalar function by using the conjugate gradient method. By imposing a position constraint as a regularization term in the objective function, we can construct the best-fitted fault surfaces by extracting zero isosurfaces from this scalar function.

Instead of directly solving an implicit scalar function in PESM, PSSM constructs fault surfaces by locally fitting an algebraic sphere at each seismic image point in a moving least-squares method. By separately minimizing the position and orientation constraint schemes, the algebraic spherical coefficient vector can be explicitly solved everywhere in the seismic image. Then, the scalar function is estimated as the algebraic distance between every seismic sample to the corresponding spherical surface constructed as spherical coefficient vector. Finally, the fault surfaces are represented by the zero isosurfaces extracted from the implicit scalar function.

Both approaches fit the fault samples globally so that they are highly resilient to noise. However, the challenge still remains in constructing branch fault surfaces in which faults with multiple orientations intersect with each other. Thus, we further propose to first classify the fault samples of crossing faults into different groups and then independently construct the crossing fault surfaces. Specifically, to eliminate spurious distortions near the fault intersections, we introduce DBSCAN to automatically classify the fault samples and make sure each cluster of samples has similar orientation features. Then, we take each cluster as the input to separately perform PESM or PSSM and hence avoid directly constructing intersecting surfaces. The continuous and complete fault surfaces obtained from our methods can be well used in following the structural interpretation and geologic modeling.

ACKNOWLEDGMENTS

This research was supported by the National Science Foundation of China under grant no. 41974121.

DATA AND MATERIALS AVAILABILITY

Data associated with this research are available and can be obtained by contacting the corresponding author.

REFERENCES

Admasu, F., S. Back, and K. Toennies, 2006, Autotracking of faults on 3D seismic data: Geophysics, **71**, no. 6, A49–A53, doi: 10.1190/1.2358399.

Al-Dossary, S., and K. J. Marfurt, 2006, 3D volumetric multispectral estimates of reflector curvature and rotation: Geophysics, **71**, no. 5, P41–P51, doi: 10.1190/1.2242449.

Alexa, M., J. Behr, D. Cohen-Or, S. Fleishman, D. Levin, and C. T. Silva, 2003, Computing and rendering point set surfaces: IEEE Transactions on Visualization and Computer Graphics, **9**, 3–15, doi: 10.1109/TVCG.2003.1175093.

Aqrawi, A. A., and T. H. Boe, 2011, Improved fault segmentation using a dip guided and modified 3D Sobel filter: 81st Annual International Meeting, SEG, Expanded Abstracts, 999–1003, doi: 10.1190/1.3628241.

Caumon, G., P. Collon-Drouaillet, C. Le Carlier de Veslud, S. Viseur, and J. Sausse, 2009, Surface-based 3D modeling of geological structures: Mathematical Geosciences, **41**, 927–945, doi: 10.1007/s11004-009-9244-2.

Di, H., and D. Gao, 2014a, Gray-level transformation and canny edge detection for 3D seismic discontinuity enhancement: Computers and Geosciences, **72**, 192–200, doi: 10.1016/j.cageo.2014.07.011.

Di, H., and D. Gao, 2014b, A new algorithm for evaluating 3D curvature and curvature gradient for improved fracture detection: Computers and Geosciences, **70**, 15–25, doi: 10.1016/j.cageo.2014.05.003.

Di, H., and D. Gao, 2016, Efficient volumetric extraction of most positive/negative curvature and flexure for fracture characterization from 3D seismic data: Geophysical Prospecting, **64**, 1454–1468, doi: 10.1111/1365-2478.12350.

Di, H., M. Shafiq, and G. AlRegib, 2018, Patch-level MLP classification for improved fault detection: 88th Annual International Meeting, SEG, Expanded Abstracts, 2211–2215, doi: 10.1190/segam2018-2996921.1.

Ester, M., 1996, A density-based algorithm for discovering clusters in large spatial databases with noise: Proceedings of the International Conference on Knowledge Discovery and Data Mining.

Gibson, D., M. Spann, J. Turner, and T. Wright, 2005, Fault surface detection in 3-D seismic data: IEEE Transactions on Geoscience and Remote Sensing, **43**, 2094–2102, doi: 10.1109/TGRS.2005.852769.

Guennebaud, G., M. Germann, and M. Gross, 2008, Dynamic sampling and rendering of algebraic point set surfaces: Computer Graphics Forum, Wiley Online Library, 653–662.

Guennebaud, G., and M. Gross, 2007, Algebraic point set surfaces: Presented at the ACM SIGGRAPH.

Guitton, A., 2018, 3D convolutional neural networks for fault interpretation: 80th Annual International Conference and Exhibition, EAGE, Extended Abstracts, 1–5.

Hale, D., 2013, Methods to compute fault images, extract fault surfaces, and estimate fault throws from 3D seismic images: Geophysics, **78**, no. 2, O33–O43, doi: 10.1190/geo2012-0331.1.

Huang, L., X. Dong, and T. E. Clee, 2017, A scalable deep learning platform for identifying geologic features from seismic attributes: The Leading Edge, **36**, 249–256, doi: 10.1190/tle36030249.1.

Kadlec, B. J., G. A. Dorn, H. M. Tufo, and D. A. Yuen, 2008, Interactive 3-D computation of fault surfaces using level sets: Visual Geosciences, **13**, 133–138, doi: 10.1007/s10069-008-0016-9.

Kazhdan, M., M. Bolitho, and H. Hoppe, 2006, Poisson surface reconstruction: Proceedings of the Fourth Eurographics Symposium on Geometry Processing.

Kazhdan, M., and H. Hoppe, 2013, Screened Poisson surface reconstruction: ACM Transactions on Graphics, **32**, 1, doi: 10.1145/2487228.2487237.

Li, F., and W. Lu, 2014, Coherence attribute at different spectral scales: Interpretation, **2**, no. 1, SA99–SA106, doi: 10.1190/INT-2013-0089.1.

Lorensen, W. E., and H. E. Cline, 1987, Marching cubes: A high resolution 3D surface construction algorithm: ACM SIGGRAPH Computer Graphics, 163–169.

Lou, Y., B. Zhang, T. Lin, N. Liu, H. Wu, R. Liu, and D. Cao, 2019a, Accurate seismic dip and azimuth estimation using semblance dip guided structure tensor analysis: Geophysics, **84**, no. 5, O103–O112, doi: 10.1190/geo2018-0530.1.

Lou, Y., B. Zhang, R. Wang, T. Lin, and D. Cao, 2019b, Seismic fault attribute estimation using a local fault model: Geophysics, **84**, no. 4, O73–O80, doi: 10.1190/geo2018-0678.1.

Marfurt, K. J., R. L. Kirlin, S. L. Farmer, and M. S. Bahorich, 1998, 3-D seismic attributes using a semblance-based coherency algorithm: Geophysics, **63**, 1150–1165, doi: 10.1190/1.1444415.

Marfurt, K. J., V. Sudhaker, A. Gersztenkorn, K. D. Crawford, and S. E. Nissen, 1999, Coherency calculations in the presence of structural dip: Geophysics, **64**, 104–111, doi: 10.1190/1.1444508.

Pedersen, S. I., T. Randen, L. Sonneland, and Ø. Steen, 2002, Automatic fault extraction using artificial ants: 72nd Annual International Meeting, SEG, Expanded Abstracts, 512–515, doi: 10.1190/1.1817297.

Pedersen, S. I., T. Skov, A. Hetlelid, P. Fayemendy, T. Randen, and L. Sønneland, 2003, New paradigm of fault interpretation: 73rd Annual International Meeting, SEG, Expanded Abstracts, 350–353, doi: 10.1190/1.1817918.

Pedregosa, F., G. Varoquaux, A. Gramfort, V. Michel, B. Thirion, O. Grisel, M. Blondel, P. Prettenhofer, R. Weiss, V. Dubourg, J. Vanderplas, A. Passos, D. Cournapeau, M. Brucher, M. Perrot, and E. Duchesnay, 2011, Scikit-learn: Machine learning in Python: Journal of Machine Learning Research, **12**, 2825–2830.

Pratt, V., 1987, Direct least-squares fitting of algebraic surfaces: ACM SIGGRAPH Computer Graphics, 145–152.

Qi, J., and J. Castagna, 2013, Application of a PCA fault-attribute and spectral decomposition in Barnett shale fault detection: 83rd Annual International Meeting, SEG, Expanded Abstracts, 1421–1425, doi: 10.1190/segam2013-0674.1.

Qi, J., F. Li, and K. Marfurt, 2017a, Multiazimuth coherence: Geophysics, **82**, no. 6, O83–O89, doi: 10.1190/geo2017-0196.1.

Qi, J., B. Lyu, A. AlAli, G. Machado, Y. Hu, and K. Marfurt, 2018, Image processing of seismic attributes for automatic fault extraction: Geophysics, **84**, no. 1, O25–O37, doi: 10.1190/geo2018-0369.1.

Qi, J., G. Machado, and K. Marfurt, 2017b, A workflow to skeletonize faults and stratigraphic features: Geophysics, **82**, no. 4, O57–O70, doi: 10.1190/geo2016-0641.1.

Ramasubramanian, V., and K. K. Paliwal, 1992, Fast k-dimensional tree algorithms for nearest neighbor search with application to vector quantization encoding: IEEE Transactions on Signal Processing, **40**, 518–531, doi: 10.1109/78.120795.

Randen, T., S. I. Pedersen, and L. Sønneland, 2001, Automatic extraction of fault surfaces from three-dimensional seismic data: 81st Annual International Meeting, SEG, Expanded Abstracts, 551–554, doi: 10.1190/1.1816675.

Roberts, A., 2001, Curvature attributes and their application to 3D interpreted horizons: First break, **19**, 85–100, doi: 10.1046/j.0263-5046.2001.00142.x.

Shewchuk, J. R., 1994, An introduction to the conjugate gradient method without agonizing pain: Presented at the Technical Report CMU-CS-94-125, Carnegie-Mellon University.

Van Bemmel, P. P., and R. E. Pepper, 2000, Seismic signal processing method and apparatus for generating a cube of variance values: U. S. Patent 6,151,555.

Wu, X., and S. Fomel, 2018, Automatic fault interpretation with optimal surface voting: Geophysics, **83**, no. 5, O67–O82, doi: 10.1190/geo2018-0115.1.

Wu, X., and D. Hale, 2016, 3D seismic image processing for faults: Geophysics, **81**, no. 2, IM1–IM11, doi: 10.1190/geo2015-0380.1.

Wu, X., L. Liang, Y. Shi, and S. Fomel, 2019a, FaultSEG3D: Using synthetic data sets to train an end-to-end convolutional neural network for 3D seismic fault segmentation: Geophysics, **84**, no. 3, IM35–IM45, doi: 10.1190/geo2018-0646.1.

Wu, X., Y. Shi, S. Fomel, L. Liang, Q. Zhang, and A. Z. Yusifov, 2019b, Faultnet3D: predicting fault probabilities, strikes, and dips with a single convolutional neural network: IEEE Transactions on Geoscience and Remote Sensing, **57**, 9138–9155, doi: 10.1109/TGRS.2019.2925003.

Xiong, W., X. Ji, Y. Ma, Y. Wang, N. M. AlBinHassan, M. N. Ali, and Y. Luo, 2018, Seismic fault detection with convolutional neural network: Geophysics, **83**, no. 5, O97–O103, doi: 10.1190/geo2017-0666.1.

Zhang, B., Y. Liu, M. Pelissier, and N. Hemstra, 2014, Semiautomated fault interpretation based on seismic attributes: Interpretation, **2**, no. 1, SA11–SA19, doi: 10.1190/INT-2013-0060.1.

Zhao, T., and P. Mukhopadhyay, 2018, A fault-detection workflow using deep learning and image processing: 88th Annual International Meeting, SEG, Expanded Abstracts, 1966–1970, doi: 10.1190/segam2018-2997005.1.

Zhou, A., S. Zhou, J. Cao, Y. Fan, and Y. Hu, 2000, Approaches for scaling DBSCAN algorithm to large spatial databases: Journal of Computer Science and Technology, **15**, 509–526, doi: 10.1007/BF02948834.

Biographies and photographs of the authors are not available.